Granular flow regimes in rotating drums from depth-integrated theory

C.-Y. Hung, C. P. Stark, and H. Capart

Granular flow regimes in rotating drums
from depth-integrated theory

C.-Y. Hung

Lamont-Doherty Earth Observatory, Columbia University. and

Department of Civil Engineering and Hydrotech

Research Institute, National Taiwan University.

C. P. Stark

Lamont-Doherty Earth Observatory, Columbia University.

H. Capart

Department of Civil Engineering and Hydrotech

Research Institute, National Taiwan University.

Abstract

Granular flows in rotating drums transition between two regimes characterized by straight and curved free surfaces. Here we predict this behavior using a depth-integrated theory applicable to general eroding flows. Closure is achieved by a local $\mu(I)$ rheology and an equation for kinetic energy. Spanning the transition, the theory yields relations for all flow properties in terms of a single dimensionless rotation rate. In accord with experiments, distinct scaling laws are obtained for slow and fast rates, dominated respectively by local energy dissipation and longitudinal energy transfer.

Granular surface flows in half-filled rotating drums are a simple analog of geophysical processes such as debris flows and rock avalanches. Like their natural counterparts, they entrain, convey, and detrain grains from an erodible substrate [1]. Unlike natural flows, their dynamics are simple to observe experimentally over a wide range of regimes produced by varying the rotation rate of the drum [2–4]. From very slow to very fast rotation rates, the flows range from intermittent to continuous to centrifugal [5, 6]. Restricting our attention to continuous, non-centrifugal avalanching, experimental flows exhibit a gradual transition between rolling and cascading regimes, characterized respectively by straight and curved free surfaces [5–8] and governed by different scaling laws [9, 10]. So far, theories have not been able to predict these flows based on rheology and mechanics alone without *ad hoc* assumptions [7, 11, 12].

In this communication, we show that the transition between rolling and cascading can be predicted from a simple depth-integrated theory applicable to general eroding flows. In this theory [13], an equation for kinetic energy completes a system of mass and momentum equations for the flowing layer. Crucially for drum flows, it captures granular entrainment and detrainment without requiring either a separate erosion law [14, 15] or a constraint on the shear rate across the layer [7, 11]. The only closures needed are a rheological law for the granular stresses, capturing their rate-dependence, and a law for wall friction accounting for the crucial role played by the sidewalls. Across the rolling to cascading transition, the theory predicts drum flow properties that compare well with experimental measurements.

Beyond this predictive ability, the theory provides new insights into the flow physics. Instead of the multiple dimensionless numbers identified earlier as potentially relevant [8, 16], the transition between rolling and cascading is found to depend on a single dimensionless rotation rate $\hat{\omega}$, expressing the strength of entrainment. Corresponding to slow and fast rates $\hat{\omega}$, rolling and cascading are associated with distinct energy dynamics. At slow rates, flows maintain a local equilibrium between production and dissipation of kinetic energy. At fast rates, longitudinal transfer of kinetic energy dominates. This produces distinct power-law asymptotes for the two regimes.

Consider a drum of width W and radius R, half-filled with dry grains of diameter D (Fig. 1(a)). When rotating the drum at constant angular velocity ω, two distinct granular regions form [2, 5]: a deep bed, undergoing rigid body rotation, and a shallow avalanching layer undergoing shear flow. We seek to predict at steady state the mean flow velocity $\overline{u}(x)$
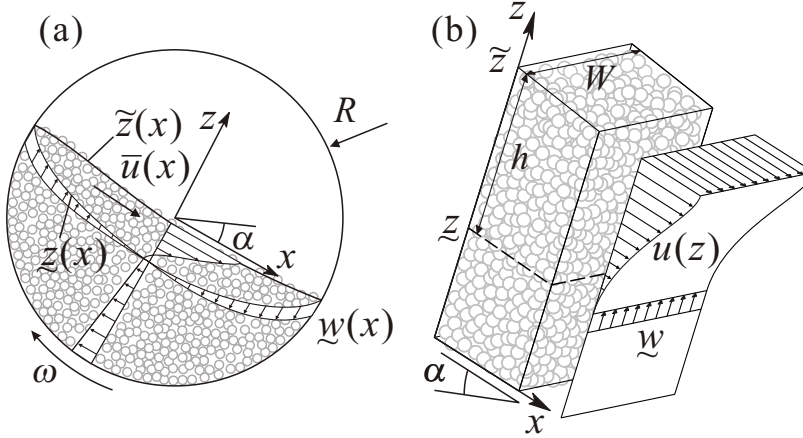
FIG. 1. Definition sketch: (a) overview; (b) local cutaway.

and the top and bottom boundaries $\widetilde{z}(x)$ and $\underset{\sim}{z}(x)$ of the avalanching layer. Whereas no flux occurs across the free surface $\widetilde{z}(x)$, the basal interface $\underset{\sim}{z}(x)$ is a yield locus across which grains are continuously entrained and detrained at rate $\underset{\sim}{w}(x) = -\omega x$. Since there are three unknown profiles $\overline{u}(x)$, $\widetilde{z}(x)$ and $\underset{\sim}{z}(x)$, two balance equations for mass and momentum are not sufficient [17]. Recently, we proposed to complete the description by deriving a third balance law for the kinetic energy of the flowing layer. For steady flow, this yields the three depth-integrated equations [13]:

$$\frac{\mathrm{d}}{\mathrm{d}x}\left(h\overline{u}\right) = \underset{\sim}{w}\,,\tag{1}$$

$$\frac{\mathrm{d}}{\mathrm{d}x}\left(\tfrac{77}{48}h\overline{u}^2\right) = -g_\perp h\frac{\mathrm{d}\widetilde{z}}{\mathrm{d}x} - \frac{\mu_W}{W}g_\perp h^2\,,\tag{2}$$

$$\frac{\mathrm{d}}{\mathrm{d}x}\left(\kappa h\overline{u}^3\right) = -g_\perp h\overline{u}\frac{\mathrm{d}\widetilde{z}}{\mathrm{d}x} - \tfrac{5}{9}\frac{\mu_W}{W}g_\perp h^2\overline{u} - \tfrac{35}{9}\chi Dg_\perp^{1/2}\frac{\overline{u}^2}{h^{1/2}}\,.\tag{3}$$

Derived subject to the shallow flow approximation ($h/R << 1$), these are balance equations for the mass, momentum, and kinetic energy of the flowing layer, integrated over the width W and depth $h(x) = \widetilde{z}(x) - \underset{\sim}{z}(x)$ (Fig. 1). For example, eq. (1) results from integrating the local continuity equation $\partial u/\partial x + \partial w/\partial z = 0$ from $\underset{\sim}{z}$ to $\widetilde{z}$, subject to the kinematic boundary conditions $\underset{\sim}{u} = 0$ and $\underset{\sim}{w} = -\omega x$ along the basal interface, and $\widetilde{w} = \widetilde{u}\,\partial\widetilde{z}/\partial x$ along the free surface. The forces considered in eqs (2) and (3) are those resulting from gravity, friction along the side walls, and internal granular stresses (see [13, 18] for detailed derivations). The coordinate x is measured along a straight axis tilted at the granular angle of repose α, with origin $x = 0$ at the drum center, and $g_\perp = g\cos\alpha$ is the component of gravity normal to the x axis. Constitutive parameters μ_W and χ are respectively the wall friction coefficient and

the slope of the linearized $\mu(I)$ rheology adopted to model the granular stresses [19–22]:

$$\tau_{xz} = \mu(I)\sigma = (\mu_0 + \chi I)\sigma \,, \tag{4}$$

where τ_{xz} is the shear stress, $I = \dot{\gamma}_{xz}D\sqrt{\rho/\sigma}$ the inertial number, $\dot{\gamma}_{xz}$ the shear rate, $\mu_0 = \tan\alpha$ the stress ratio at yield, $\sigma = \rho g_\perp(\widetilde{z}-z)$ the granular pressure, assumed lithostatic, and $\rho = c_S\rho_S$ the bulk density. In (4), the first rate-independent term $\mu_0\sigma$ is the Coulomb yield stress, which vanishes from (2,3) because of the tilted coordinate system. The second, rate-dependent term $\chi I\sigma$ represents a granular-viscous contribution, with a pressure-dependent effective viscosity.

In (2) and (3) the left-hand terms are the momentum and kinetic energy fluxes. On the right hand sides, the first terms are the force and work of the pressure gradient, and the second terms the force and energy dissipation due to wall friction. The last term of (3) is a key term with no counterpart in (2), representing energy dissipation by the granular-viscous stress. In (2,3), the coefficients $\frac{77}{48}$, $\kappa = \frac{342853}{233376} \approx 1.469$, $\frac{5}{9}$ and $\frac{35}{9}$ are obtained from moments of the self-similar velocity profile produced by the rheology for steady uniform heap flow [13, 19, 23]. This depth-wise profile is given by (Fig.1(b)):

$$\frac{u(x,z)}{\overline{u}(x)} = \tfrac{7}{3} - \tfrac{35}{6}\hat{\eta}^{3/2} + \tfrac{7}{2}\hat{\eta}^{5/2} \,, \tag{5}$$

where $\hat{\eta}(x,z) = (\widetilde{z}(x) - z)/h(x)$, and allows the full velocity field to be reconstructed from long profiles $\overline{u}(x)$, $\widetilde{z}(x)$ and $\underline{z}(x)$.

Choosing the drum rotation rate ω as the principal control variable and setting $\hat{x} = x/R$, the response variables h, $\overline{u}$ and $S = -\mathrm{d}\widetilde{z}/\mathrm{d}x$ can be normalized independently of ω in the form $\hat{h} = h/h_c$, $\overline{\hat{u}} = \overline{u}/\overline{u}_c$, and $\hat{S} = S/S_c$ where the expressions for h_c, $\overline{u}_c$, and S_c are given in Table I. On normalizing in this way, the response depends on the single dimensionless number

$$\hat{\omega} = \frac{\omega R^{9/8}(W/\mu_W)^{1/8}}{g_\perp^{1/2}(\chi D)^{3/4}} \,. \tag{6}$$

Physically, the dimensionless rotation rate $\hat{\omega}$ can be interpreted as the ratio of the forced entrainment rate $f_c = \omega R$ to the free entrainment rate $e_c = h_c/t_c$ obtained for uniform unsteady flows, where $t_c = h_c^{3/2}/(g_\perp^{1/2}\chi D)$ is the time scale over which unsteady entrainment occurs [13]. For zero entrainment ($\hat{\omega} = 0$), the solution is a steady uniform flow in equilibrium with excess slope $\hat{S}$. The parameter $\hat{\omega}$ therefore measures how strongly entrainment perturbs the flow away from local equilibrium, and we hereafter call it the *entrainment number*.

4

TABLE I. Characteristic variable definitions ξ_c and scaling exponents a_ξ, b_ξ for asymptotic regimes $\mathcal{R}_a$ ($\hat\omega \to 0$) and $\mathcal{R}_b$ ($\hat\omega \to \infty$). For any given variable ξ, we denote by $\hat\xi = \xi/\xi_c$ its dimensionless value, and by $\hat\xi \propto \hat\omega^{a_\xi}$ or $\hat\xi \propto \hat\omega^{b_\xi}$ its asymptotic scaling law.

ξ	ξ_c	a_ξ	b_ξ
h	$(\chi D)^{1/2} R^{1/4} (W/\mu_W)^{1/4}$	2/7	2/3
$\overline{u}$	$g_\perp^{1/2} (\chi D)^{1/4} R^{5/8} (W/\mu_W)^{-3/8}$	5/7	1/3
S	$(\chi D)^{1/2} R^{1/4} (W/\mu_W)^{-3/4}$	2/7	2/3
A	$h_c R$	2/7	2/3
K	$h_c \overline{u}_c^2 R$	12/7	4/3
Φ	$g_\perp^{1/2} (\chi D) h_c^{-1/2} \overline{u}_c^2 R$	9/7	1/3

Subject to the above assumptions, this number $\hat\omega$ is the sole control parameter for granular flows in half-filled drums.

Further insight can be obtained by examining the two asymptotic regimes $\mathcal{R}_a$ and $\mathcal{R}_b$ resulting from defining $\hat h_a = h/h_a$, $\hat h_b = h/h_b$ etc., then assuming the power law scalings $h_a = \hat\omega^{a_h} h_c$, $h_b = \hat\omega^{b_h} h_c$ etc., with exponents a_h, b_h etc., selected to balance particular terms in equations (1)-(3) (see Table I). For both regimes, we first set $a_h + a_u = b_h + b_u = 1$ to balance the two sides of continuity equation (1). For regime $\mathcal{R}_a$, we then equilibrate the right-hand terms of (2) and (3) to obtain the dimensionless equations

$$\hat\omega^{8/7} \frac{\mathrm{d}}{\mathrm{d}\hat x} \left(\tfrac{77}{48} \hat h_a \overline{\hat u}_a^2 \right) = \hat h_a \hat S_a - \hat h_a^2 \,, \tag{7}$$

$$\hat\omega^{8/7} \frac{\mathrm{d}}{\mathrm{d}\hat x} \left(\kappa \hat h_a \overline{\hat u}_a^3 \right) = \hat h_a \overline{\hat u}_a \hat S_a - \tfrac{5}{9} \hat h_a^2 \overline{\hat u}_a - \tfrac{35}{9} \hat h_a^{-1/2} \overline{\hat u}_a^2 \,. \tag{8}$$

In the limit $\hat\omega \to 0$, the left-hand terms associated with convective inertia are found to vanish. Adopting the $\mathcal{R}_a$ scalings (see Table I) therefore produces $\hat\omega$-independent equations in the limit of low entrainment numbers. In this limit, the momentum and kinetic energy fluxes play no role and the flow layer balances momentum and kinetic energy locally. Flow depth, mean velocity, and excess inclination consequently exhibit the simple scaling laws $\hat h \propto \hat\omega^{2/7}$, $\overline{\hat u} \propto \hat\omega^{5/7}$, and $\hat S \propto \hat\omega^{2/7}$.

For regime $\mathcal{R}_b$, we balance all terms of (2) and (3), with the exception of the last right-hand term of (3) associated with dissipation by granular-viscous stresses. This produces the

new dimensionless equations

$$\frac{\mathrm{d}}{\mathrm{d}\hat{x}}\left(\tfrac{77}{48}\hat{h}_b\overline{\hat{u}}_b^2\right) = \hat{h}_b\hat{S}_b - \hat{h}_b^2\,, \tag{9}$$

$$\frac{\mathrm{d}}{\mathrm{d}\hat{x}}\left(\kappa\hat{h}_b\overline{\hat{u}}_b^3\right) = \hat{h}_b\overline{\hat{u}}_b\hat{S}_b - \tfrac{5}{9}\hat{h}_b^2\overline{\hat{u}}_b - \left(\frac{1}{\hat{\omega}}\right)^{4/3}\tfrac{35}{9}\hat{h}_b^{-1/2}\overline{\hat{u}}_b^2\,. \tag{10}$$

Now the last term of (10) vanishes in the limit $\hat{\omega}\to\infty$. Adopting the $\mathcal{R}_b$ scalings (see Table I) leads to $\hat{\omega}$-independent equations in the limit of high rotation rates. In this limit, granular-viscous dissipation exerts no influence. Instead, the pressure gradient and wall friction are balanced by convective inertia, hence the left-hand momentum and kinetic energy fluxes play dominant roles. For this asymptote, the flow depth, mean velocity, and excess inclination vary with rotation rate according to the scaling laws $\hat{h}\propto\hat{\omega}^{2/3}$, $\overline{\hat{u}}\propto\hat{\omega}^{1/3}$, and $\hat{S}\propto\hat{\omega}^{2/3}$.

In the limits of low and high entrainment numbers, we thus obtain two asymptotic regimes characterized by distinct power-law exponents. By solving equations (1)-(3), we can also calculate flow profiles, and capture the gradual transition between the two regimes. For arbitrary entrainment number $\hat{\omega}$, solutions to the equations are obtained as follows. Integration of (1) first yields the granular discharge $q(x) = h(x)\overline{u}(x) = \frac{1}{2}\omega(R^2-x^2)$ [5]. The excess slope $S = -\mathrm{d}\widetilde{z}/\mathrm{d}x$ is then eliminated between (2) and (3), to produce a single non-linear ordinary differential equation for the depth profile $h(x)$. In dimensionless variables, this ODE reads

$$\frac{\mathrm{d}\hat{h}}{\mathrm{d}\hat{x}} = \frac{560\hat{h}^{1/2}\hat{q} - 64\hat{h}^4 + 6\hat{\omega}^{7/8}(72\kappa - 77)\hat{h}\hat{q}\,\mathrm{d}\hat{q}/\mathrm{d}\hat{x}}{3\hat{\omega}^{7/8}(96\kappa - 77)\hat{q}^2}\,, \tag{11}$$

where $\hat{h}(\hat{x})$ is the unknown depth profile and $\hat{q}(\hat{x}) = \frac{1}{2}\hat{\omega}(1 - \hat{x}^2)$ is the prescribed discharge profile, both in dimensionless form. The solution curve $\hat{h}(\hat{x})$ can then integrated numerically starting from upstream boundary condition $\hat{h}(-1) = 0$. When both $\hat{h}$ and $\hat{q}$ are greater than 0 (away from the upstream and downstream ends $\hat{x} = \mp 1$), the right-hand-side is well-behaved and simple to integrate. Care is required at the two ends, however, where both $\hat{h}$ and $\hat{q}$ tend to zero and the solution curve features vertical tangents. For low values of $\hat{\omega}$, the ODE becomes stiff and difficult to solve numerically. Fortunately the solution curve in the limit $\hat{\omega}\to 0$ can be found analytically and is given by $\hat{h}(\hat{x}) = (\tfrac{35}{4}\hat{q}(\hat{x}))^{2/7}$. Once the depth profile $h(x)$ is obtained, the excess slope profile $S(x) = -\mathrm{d}\widetilde{z}/\mathrm{d}x$ is also known. Subject to the integral condition $\int_{-R}^{R}\widetilde{z}(x)\mathrm{d}x = 0$ (expressing mass conservation), this slope profile can finally be integrated to obtain the surface shape profile $\widetilde{z}(x)$.

To check the theory, we conducted rotating drum experiments in which the full granular velocity field was measured with precision. Two sets of spherical, mildly polydisperse aluminosilicate millstones ($\rho_S = 2610 \text{ kg m}^{-3}$) with different mean grain diameters $D_1 = 2.3$ mm and $D_2 = 4.1$ mm respectively were used to half-fill a drum of radius $R = 200$ mm and width $W = 40$ mm with aluminum and glass walls on either side. Experiments were restricted to the range $5 \times 10^{-5} < \text{Fr} < 0.3$, where $\text{Fr} = R\omega^2/g$ is the Froude number or ratio of centrifugal to gravitational acceleration. Below the lower bound, intermittent avalanching is observed in our experimental system. Above the upper bound, on the other hand, centrifugal effects can be expected to play a dominant role [6]. Applicability of the proposed theory is therefore restricted to the selected range.

The constitutive coefficients of the theory were estimated from independent experimental tests. Grain-wall friction coefficients $\mu_A = 0.26$ and $\mu_G = 0.21$ were measured in slider tests yielding a mean of $\mu_W = 0.24$. For the same grains, steady uniform heap flows were used in [13] to calibrate coefficient values $\mu_0 = 0.33$ and $\chi = 0.52$ for the linearized $\mu(I)$ rheology (4), and we adopt these values without adjustment for the comparisons below. A high speed video camera and particle tracking velocimetry were used to record and track grain motions at millisecond intervals through the glass sidewall [24]. Grain displacement vectors gathered over several seconds of flow were converted into time-averaged velocity fields and streamfunctions Ψ over a 1 mm-resolution Cartesian grid. Using the dimensionless streamfunction $\hat{\Psi} = \Psi/(\frac{1}{2}\omega R^2)$, experimental surface and basal interfaces $\widetilde{z}$ and $\underset{\sim}{z}$ were then inferred from the respective loci $\hat{\Psi} = 0.01$ and $\hat{\Psi} - \hat{\Psi}_0 = 0.02$, where $\Psi_0 = \frac{1}{2}\omega(R^2 - x^2 - z^2)$ is the streamfunction associated with solid body rotation alone.

Measured and predicted results are presented in Fig.2 for diameter D_1 and the two rotation rates $\omega = 1$ rpm and $\omega = 10$ rpm. These correspond to entrainment numbers $\hat{\omega} = 0.7$ and $\hat{\omega} = 7$, and display the distinct signatures of the rolling and cascading regimes [5, 7, 8]. In the rolling regime (Fig.2(a),(c)) the avalanching layer adopts a lenticular thickness profile $h(x)$ and a nearly straight free surface $\widetilde{z}(x)$ (black lines). In the cascading regime (Fig.2(b),(d)), by contrast, the layer acquires an asymmetric thickness profile, blunt upstream but cusped downstream, and a curved free surface. The largest velocity magnitudes (in color), focused near the free surface, are symmetric with respect to the drum center for the rolling regime, but displaced downstream for the cascading regime. Finally the streamlines (white contours) show clearly how grains trapped in the slowly rotated deposits are
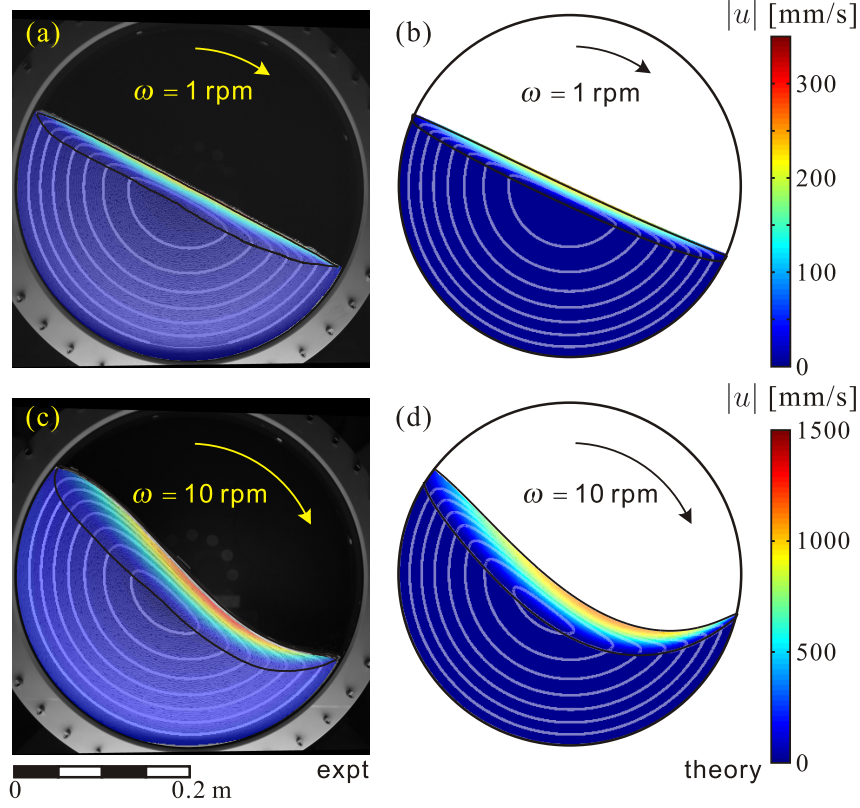
7

FIG. 2. Comparison of measured (a,c) and predicted flow fields (b,d) for low and high entrainment numbers: (a,b) $\hat{\omega} = 0.7$; (c,d) $\hat{\omega} = 7$. Color: velocity magnitude; black profiles: free surface and basal interface; white contours: streamlines from level sets of the dimensionless streamfunction $\hat{\Psi}$ at equally spaced values. For the predicted streamlines on panels (b) and (d), we added a correction $\Delta\Psi = -\frac{1}{2}\omega z^2$ to the streamfunction Ψ deduced from the theory, to add back the small velocity component $u_0 = -\partial\Psi_0/\partial z$ due to solid body rotation and neglected by our shallow flow approximation.

fed back to the rapidly avalanching surface flows. For all these features, good qualitative agreement is obtained between the measured and predicted flow fields. The level of quantitative agreement, however, is not sufficient to collapse predicted and measured profiles on the same plot.

To visualize the energy dynamics of the two regimes, color grids in Fig.3(a)-(d) illustrate spatial distributions of the quantity

$$\varphi(x,z) = \frac{\partial}{\partial x_j}\left(\tfrac{1}{2}|u|^2 u_j\right) + \chi D(\sigma/\rho)^{1/2}|\dot{\gamma}|^2 \, , \tag{12}$$

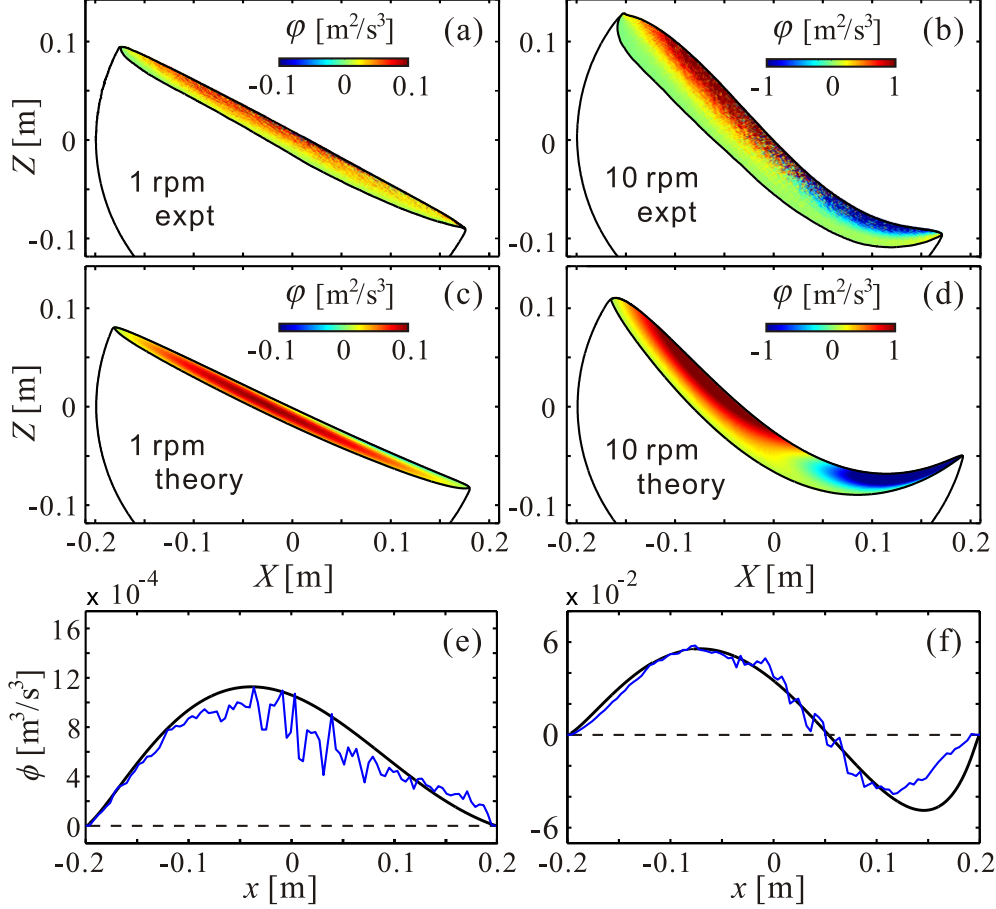equal to the sum of two terms: the divergence of the kinetic energy flux and the dissipation

8

FIG. 3. Visualization of the energy dynamics at low and high entrainment numbers $\hat{\omega} = 0.7$ (left) and $\hat{\omega} = 7$ (right): (a),(b) measured $\varphi(x,z)$ grids; (c),(d) predicted $\varphi(x,z)$ grids; (e),(f) measured (blue) and predicted $\phi(x)$ profiles (black). For the measured profile $\phi(x)$, the coordinate x is taken along a secant line connecting the upstream and downstream endpoints of the free surface.

by the granular-viscous stress. Here $|u|$ is the norm of the local velocity and $|\dot{\gamma}|$ is the second invariant of the shear rate tensor $\dot{\gamma}_{ij} = \partial u_i/\partial x_j + \partial u_j/\partial x_i$, where $(x_1, x_2) = (x, z)$. Consistent with the shallow flow assumption, for the theory we approximate $|u|^2 \approx u^2$ and $|\dot{\gamma}|^2 \approx \dot{\gamma}_{xz}^2$, and deduce profiles in the z-direction from the assumed self-similar shape of the velocity profile (5). For the experiments, we calculate the full expressions $|u| = \sqrt{u_k u_k}$ and $|\dot{\gamma}| = \sqrt{\dot{\gamma}_{ij}\dot{\gamma}_{ij}}$ from the measured velocity fields.

The resulting $\varphi(x,z)$ distributions demonstrate how rolling and cascading are associated with distinct energy dynamics. In the rolling regime (Fig.3(a),(c)), granular-viscous dissipation dominates over kinetic energy transfer (limit $\hat{\omega} \to 0$ of regime $\mathcal{R}_a$). Since the local

9

dissipation (second right-hand term of (12)) is positive definite, this yields a monopolar (red) φ distribution. In the cascading regime (Fig.3(b),(d)), by contrast, kinetic energy transfer dominates over viscous dissipation (limit $\hat{\omega} \to \infty$ of regime $\mathcal{R}_b$). Produced upstream, where its flux has positive divergence, kinetic energy is convected downstream where its divergence becomes negative. As kinetic energy is transported from source (red) to sink (blue), a bipolar φ distribution is obtained.

To make the comparisons more quantitative, we plot in Fig.3(e),(f) the profiles $\phi(x) = \int_{\underline{z}}^{\widetilde{z}} \varphi(x, z) \, \mathrm{d}z$ obtained by integrating $\varphi(x, z)$ over the flow depth. In the rolling regime (Fig.3(e)), the $\phi(x)$ profile is nearly symmetric about $x = 0$, as the dominant granular-viscous dissipation inherits the symmetry of the flow discharge and thickness profiles. In the cascading regime (Fig.3(f)), the source and sink due to the divergence of the kinetic energy flux dominate, and the $\phi(x)$ profile becomes nearly antisymmetric. Good agreement with the experiments is obtained, confirming that the theory correctly captures the energy dynamics for both regimes.

Figure 4 shows results from 34 drum experiments in which the rotation rate ω was varied from 1 to 30 rpm. Measurements are compared with predictions for the following quantities: the excess surface inclination $S = -\mathrm{d}\widetilde{z}/\mathrm{d}x$ at the drum centerline (Fig.4(a)), the area of the flowing layer $A = \int_{-R}^{R} (\widetilde{z} - \underline{z}) \, \mathrm{d}x$, (Fig.4(b)), the total kinetic energy $K = \int_{-R}^{R} \int_{\underline{z}}^{\widetilde{z}} |u|^2 \, \mathrm{d}z \, \mathrm{d}x$ (Fig.4(c)), and the total dissipation by viscous stresses $\Phi = \int_{-R}^{R} \phi \, \mathrm{d}x$ (Fig.4(d)). When normalized by their characteristic values S_c, A_c, K_c and Φ_c (Table I), the dimensionless quantities $\hat{S} = S/S_c$, $\hat{A} = A/A_c$, $\hat{K} = K/K_c$ and $\hat{\Phi} = \Phi/\Phi_c$ are predicted to vary with the entrainment number $\hat{\omega}$ according to universal dimensionless curves $\hat{S}(\hat{\omega})$, $\hat{A}(\hat{\omega})$, $\hat{K}(\hat{\omega})$ and $\hat{\Phi}(\hat{\omega})$ (blue lines). On the log-log graphs, the power-law asymptotes associated with regimes $\mathcal{R}_a$ ($\hat{\omega} \to 0$, in green) and $\mathcal{R}_b$ ($\hat{\omega} \to \infty$, in red) plot as straight lines with inclinations equal to their power law exponents (Table I). The dependence of $\hat{A}$ on $\hat{\omega}$, for instance, transitions from the scaling $\hat{A} \propto \hat{\omega}^{2/7}$ to the scaling $\hat{A} \propto \hat{\omega}^{2/3}$ as $\hat{\omega}$ increases. This is consistent with empirical scaling exponents obtained earlier for the dependence of the flow depth h on the rotation rate ω [9, 10]. Note that the asymptotes associated with the two regimes do not cross at the same entrainment number $\hat{\omega}$ for different quantities. Intersection points range instead from $\hat{\omega} = 2$, for the excess slope (Fig.4(a)), to $\hat{\omega} \approx 20$ for the dissipation (Fig.4(d)). Instead of a sudden change at a well-defined value of $\hat{\omega}$, the transition between rolling and cascading involves a gradual shift in the relative strength of different mechanisms. Similar
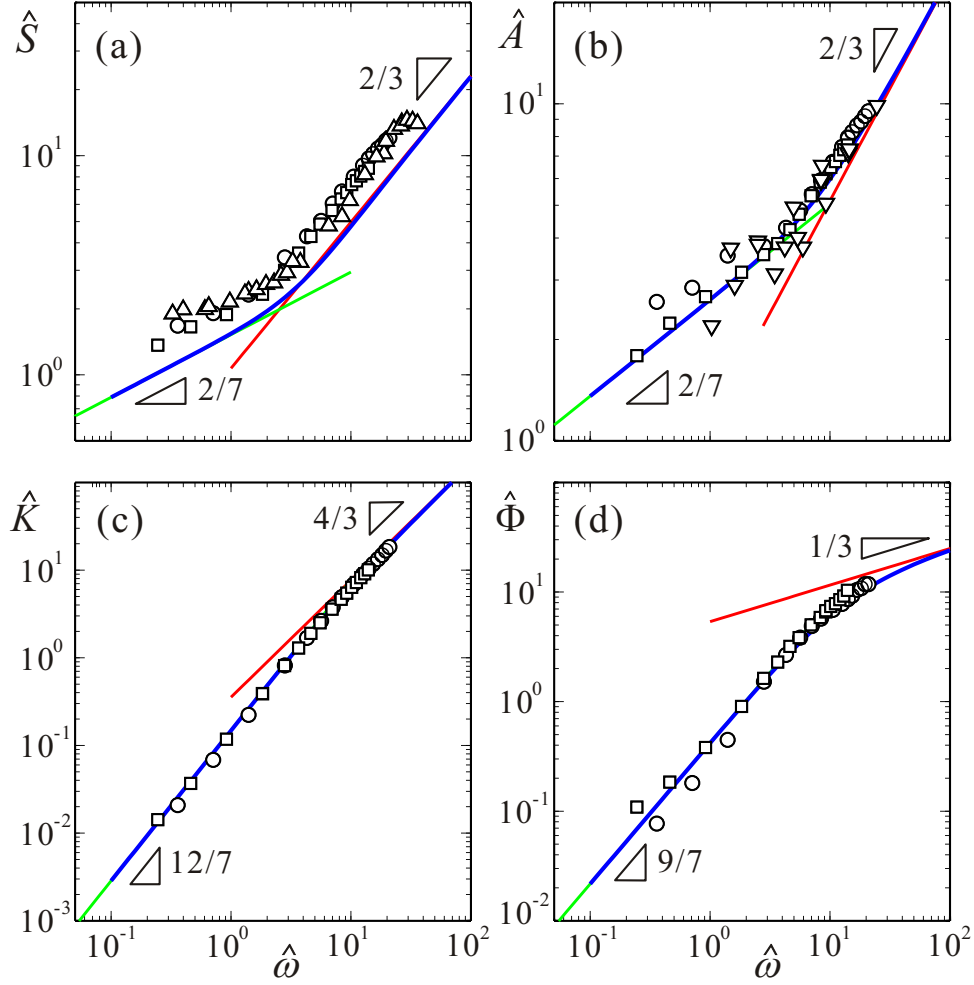
FIG. 4. Comparison of predictions and measurements for the variation with entrainment number $\hat{\omega}$ of the following quantities: (a) excess slope; (b) flow layer area; (c) total kinetic energy; (d) total viscous dissipation. Lines: theoretical curves (blue) and their low (green, regime $\mathcal{R}_a$) and high $\hat{\omega}$ asymptotes (red, regime $\mathcal{R}_b$). Symbols: our experiments for diameters D_1 (circles) and D_2 (squares), and those of [25] (deltas) and [7] (nablas).

gradual transitions between distinct power law asymptotes are well documented for heat flow between parallel plates [26].

Overall, experimental results are in reasonable agreement with the theoretical predictions. On normalization, our results for the two different grain diameters D_1 (circles) and D_2 (squares) collapse to approximate colinearity with the theoretical curves. For further comparison, slope data from [25] (deltas) and area data from [7] (nablas) are plotted in Fig.4(a) and Fig.4(b), assuming respectively the values $\mu_0 = 0.30$, $\mu_W = 0.20$, $\chi = 0.25$ and

11

$\mu_0 = 0.50$, $\mu_W = 0.20$, $\chi = 0.35$ for the constitutive coefficients. In all cases, the theory captures well both the asymptotic (green, red) and transitional responses (blue) observed in the experiments. The excess slope at the centerline, however (Fig.4(a)), is underpredicted by a constant factor of approximately 1.5, hence a constant offset in log units. The origin of this offset is unclear, but could be due to finite system size effects not modeled by the $\mu(I)$ rheology. So far, most experimental support for this rheology has come from granular heap flows in long inclined channels [13, 19, 21]. As in other finite size systems ([22]), there may be granular effects associated with the limited length of the drum system that the description does not capture, and which could cause this discrepancy. We have checked that the problem cannot be addressed simply by resetting the values of the constitutive coefficients μ_0 and χ (instead of using those calibrated from inclined channel experiments), as improving the fit for the excess slope S causes significantly poorer agreement for the flow area A and dissipation Φ.

In this communication, we have shown how a simple set of depth-integrated equations can predict avalanching flows in rotating drums based purely on rheology and mechanics. A single dimensionless parameter, the entrainment number $\hat{\omega}$, was found to govern the transition between rolling and cascading. The corresponding asymptotic regimes are dominated respectively by granular-viscous dissipation and by kinetic energy transport, yielding distinct power law exponents. These results clarify why the rotating drum has proven difficult to use as a granular rheometer [4, 9]. It turns out that, as the rotation speed increases, the influence of the rate-dependent granular rheology becomes negligible compared to the effects of convective inertia, not included in previous theories [5].

Our findings open several avenues for further investigation. In [13], the unsteady uniform version of equations (1)-(3) was found to capture well transient granular flows in tilting channels. In this communication, the equations were shown to describe steady, but spatially varying flows. It remains to test the full equations [13] for general eroding flows, variable in both space and time. The proposed equations could also support investigations of granular segregation. In [27], it was shown that for the same conditions, binary flows involving grains of two different sizes exhibit roughly the same flow field as monodisperse flows of similarly sized grains, and that segregation and mixing patterns can be modeled based on the kinematics of this flow field. Moreover, modeling is greatly facilitated when a simple description is available for the flow kinematics. By providing simple solutions for the flow

kinematics across the rolling to cascading transition, therefore, our work could provide a useful basis for modeling binary flows in the same regimes. By incorporating non-local effects absent from the $\mu(I)$ rheology [22], finally, it may become possible to extend the theory to the intermittent regime.

[1] A. Mangeney, O. Roche, O. Hungr, N. Mangold, G. Faccanoni, and A. Lucas, J. Geophys. Res. **115**, F03040 (2010).

[2] J. M. N. T. Gray, J. Fluid Mech. **441**, 1 (2001).

[3] D. V. Khakhar, A. V. Orpe, P. Andresén, and J. M. Ottino, J. Fluid Mech. **441**, 225 (2001).

[4] GDR-MIDI, Eur. Phys. J. E **14**, 341 (2004).

[5] J. Rajchenbach, Phys. Rev. Lett. **65**, 2221 (1990).

[6] J. Mellmann, Powder Tech. **118**, 251 (2001).

[7] A. V. Orpe and D. V. Khakhar, Phys. Rev. E **64**, 031302 (2001).

[8] N. Taberlet, P. Richard, and E. J. Hinch, Phys. Rev. E **73**, 050301(R) (2006).

[9] G. Félix, V. Falk, and U. D'Ortona, Eur. Phys. J. E. **22**, 25 (2007).

[10] F. Pignatel, C. Asselin, L. Krieger, I. C. Christov, J. M. Ottino, and R. M. Lueptow, Phys. Rev. E **86**, 011304 (2012).

[11] S. Douady, B. Andreotti, and A. Daerr, Eur. Phys. J. B **11**, 131 (1999).

[12] A. Aradian, E. Raphaël, and P.-G. de Gennes, C. R. Physique **3**, 187 (2002).

[13] H. Capart, C.-Y. Hung, and C. P. Stark, J. Fluid Mech. **765**, R4 (2015).

[14] L. Lê and E. B. Pitman, SIAM J. Appl. Math. **70**, 1407 (2010).

[15] F. Bouchut, E. D. Férnandez-Nieto, A. Mangeney, and P.-Y. Lagrée, Acta Mech. **199**, 181 (2008).

[16] Y. L. Ding, R. N. Forster, J. P. K. Seville, and D. J. Parker, Chem. Eng. Sci. **56**, 3737 (2001).

[17] S. Douady, B. Andreotti, A. Daerr, and P. Cladé, C. R. Physique **3**, 177 (2002).

[18] C.-Y. Hung, *Boundary erosion by granular flow: Experiments and theory*, Ph.D. thesis, National Taiwan University (2015).

[19] P. Jop, Y. Forterre, and O. Pouliquen, J. Fluid Mech. **541**, 167 (2005).

[20] F. da Cruz, S. Emam, M. Prochnow, J. Roux, and F. Chevoir, Phys. Rev. E **72**, 021309 (2005).

[21] P. Jop, Y. Forterre, and O. Pouliquen, Nature **441**, 727 (2006).

[22] D. L. Henann and K. Kamrin, Proc. Natl. Acad. Sci. U.S.A. **110**, 6730 (2013).

[23] D. Berzi and J. Jenkins, J. Fluid Mech. **608**, 393 (2008).

[24] H. Capart, D. L. Young, and Y. Zech, Exp. Fluids **32**, 121 (2002).

[25] A. Brucks, T. Arndt, J. M. Ottino, and R. M. Lueptow, Phys. Rev. E **75**, 032301 (2007).

[26] E. D. Siggia, Annu. Rev. Fluid Mech. **26**, 137 (1994).

[27] C. P. Schlick, Y. Fan, P. B. Umbanhowar, J. M. Ottino, and R. M. Lueptow, J. Fluid Mech. **765**, 632 (2015).